Tracking boundary movement and exterior shape modelling in lung EIT imaging

A. Biguri[1], A. Adler[2], B. Grychtol[3], and M. Soleimani[1]

[1]Engineering Tomography Lab (ETL), Electronic and Electrical Engineering, University of Bath, Bath, UK

[2]Systems and Computer Engineering, Carleton University, Ottawa, ON K1S 5B6, Canada

[3]Fraunhofer Project Group for Automation in Medicine and Biotechnology, 68167 Mannheim, Germany

Abstract

Electrical impedance tomography (EIT) has shown significant promise for lung imaging. One key challenge for EIT in this application is the movement of electrodes during breathing, which introduces artefacts in reconstructed images. Various approaches have been proposed to compensate for electrode movement, but no comparison of these approaches is available. This paper analyses boundary model mismatch and electrode movement in lung EIT. The aim is to evaluate the extent to which various algorithms tolerate movement, and to determine if a patient specific model is required for EIT lung imaging. Movement data are simulated from a CT-based model, and image analysis is performed using quantitative figures of merit. The electrode movement is modelled based on expected values of chest movement and an extended Jacobian method is proposed to make use of exterior boundary tracking. Results show that a dynamical boundary tracking is the most robust method against any movement, but is computationally more expensive. Simultaneous electrode movement and conductivity reconstruction algorithms show increased robustness compared to only conductivity reconstruction. The results of this comparative study can help develop a better understanding of the impact of shape model mismatch and electrode movement in lung EIT.

1 Introduction

Electrical impedance tomography (EIT) attempts to reconstruct the changes in conductivity distribution in a volume by measuring the voltage on its boundary induced by injected currents. Due to its high temporal resolution and potentially low cost hardware it is of significant interest to industrial and medical applications[1]. It is known that the shape mismatch and electrode movement in EIT are key sources of error in image reconstruction[2]. Due to the ill-posedness of the EIT inverse problem, these errors can result in artefacts in conductivity reconstruction. In medical EIT, shape mismatch can occur due to the complex geometry of the imaging region. In particular, in lung EIT, the shape will also change during data acquisition, so electrode movement is also a source of error. Both effects are commonly present in EIT lung imaging and in this work they are analysed quantitatively. To reduce the artefacts due to the electrode movement, a simultaneous electrode movement and conductivity change reconstruction method was proposed by Soleimani *et al* [3]. Some analysis on how much the breathing movement affects the reconstruction has been studied by Zhang *et al* [4] [5] and Adler *et al* [6]. Additionally, to measure the quality of EIT images, performance figures of merit were defined by Adler *et al*[7]. Various conductivity reconstruction methods were tested for a range of approximated boundary shapes by Grychtol *et al*[8] using these performance figures of merit. They concluded that above 4% shape mismatch between the known model and real geometry, the errors increase highly, therefore an accurate geometry should be used for EIT reconstruction. A more complete analysis of the shape mismatch and electrode movement reconstruction for the case of supine human breathing is proposed in this work, motivated in part by the electrode movement measurement in patients performed by Zhang *et al* [4].

The additional questions that are to be answered here are as follows: How big is the effect of boundary movement due to breathing in EIT lung imaging? In other words, how much of the signal in EIT lung images results from boundary movement alone? Do simultaneous movement and conductivity change reconstruction algorithms tolerate higher electrode movement? Would a shape tracking device be useful as a complementary device to lung EIT? Is it possible to use the information from a tracking device in image reconstruction?

With those questions in mind an analysis was performed using a number of possible methods. The paper proceeds as follows. First the four reconstruction algorithms are presented: standard Tikhonov conductivity reconstruction, simultaneous conductivity and electrode movement reconstruction with two variants in regularization scheme and standard Tikhonov scheme that uses the information from a tracked boundary. Second, the image analysis methods are briefly introduced. Subsequently, a simulation of supine position human breathing is performed to test the performance of the algorithms against expected boundary change due to human breathing. The test is repeated by assuming only approximate knowledge of the initial shape, allowing errors due to electrode movement and shape mismatch. Conclusions are draw based on statistical data analysis of a wide range of figures of merit.

2 Methods

2.1 Image reconstruction methods

The EIT image reconstruction used in this study is based on a finite element model (FEM) of the medium, discretized into n_N elements. The system has n_E electrodes obtaining n_M measurements in n_D spatial dimensions . The reconstruction is based on time difference imaging, so it reconstructs the difference between measured data $\mathbf{v}_{t_1}$ and $\mathbf{v}_{t_2}$, acquired at time t_1 and t_2, being the difference vector $\mathbf{z} = \mathbf{v}_{t_2} - \mathbf{v}_{t_1}$. Difference EIT assumes that the difference measurements are a function only of the conductivity change $\Delta\sigma = \sigma_{t_2} - \sigma_{t_1}$. The forward solution of the time difference of measurements $\mathbf{z}$ is computed with an operator F, based on a FEM model, relative to an homogeneous conductivity distribution σ_h at time t_1:

$$\mathbf{z} = F(\Delta\sigma)\Big|_{\sigma_h} . \tag{1}$$

The image reconstruction is formulated in a *maximum a posteriori* (MAP) approach[9], that computes the most likely conductivity distribution given the measurements assuming that the image properties can be modelled by a normal distribution. The function to minimize is then:

$$\hat{\mathbf{x}} = \arg\min_{\Delta\sigma} \left[(\mathbf{z} - F(\Delta\sigma))^t \Sigma_n^{-1} (\mathbf{z} - F(\Delta\sigma)) + (\Delta\sigma - \Delta\sigma_\infty)^t \Sigma_{\Delta\sigma}^{-1} (\Delta\sigma - \Delta\sigma_\infty) \right] \tag{2}$$

where $\Delta\sigma_\infty$ represents the expected value. In difference imaging, the image is not expected to change,

therefore $\Delta\sigma_\infty = 0$. The $\Sigma_{\Delta\sigma}^{-1}$ and Σ_n^{-1} are the *a priori* estimates of the image and measurement noise covariances. $\hat{\mathbf{x}}$ represents the reconstructed image.

Based on the calculation of the Jacobian, a linear approximation $F(\Delta\sigma) = \mathbf{J}\Delta\sigma$ is used, so equation (2) can be interpreted as a one-step linear inverse solution[10]

$$\hat{\mathbf{x}} = (\mathbf{J}^t\mathbf{J} + \lambda^2\mathbf{R})^{-1}\mathbf{J}^t\mathbf{z}. \tag{3}$$

if the *a priori* estimate of the image $\Sigma_{\Delta\sigma}^{-1}$, is interpreted as a regularization matrix, $\lambda^2\mathbf{R}$, where λ is the hyperparameter, a user defined value that defines the trade-off between the expected solution (the a priori estimate) and the possible solutions. The measurement noise is assumed to be uniform, therefore $\Sigma_n^{-1} = I$,

In the following sections the four used algorithms are presented briefly. The choice of hyperparameter has been set up between algorithms using the invariant noise figure (NF, defined below) method[11]. The choice of the specific value of NF comes from Crabb *et al*[12]. In their study a wide analysis of the best hyperparameter for an algorithm similar to the Tikhonov simultaneous reconstruction (defined in section 2.1.2) is performed using mutual information. In our work the numerical values chosen by Crabb *et al* are used for the Tikhonov simultaneous reconstruction approach, and the NF calculated from there, giving $NF = 0.3$.. With this NF the hyperparameters for each of the other algorithms is calculated.

2.1.1 Standard Tikhonov

One the most widely used regularization scheme for EIT is standard Tikhonov regularization, that gives preference to solutions with a smaller norm. The standard Tikhonov regularization is formulated by setting $\mathbf{R}$ in equation 3 to $\mathbf{R} = I$. In this work the value of hyperparameter (λ) has been set to 0.01 for this method. This method is referred to from now on as "Standard Tikhonov".

2.1.2 Simultaneous reconstruction methods

The main motivation for simultaneous reconstruction is to reduce the artefacts created by electrode position and boundary shape mismatches without the need of any external measuring device. The methods presented here are the same as [3], but using different regularization approaches.

In simultaneous reconstruction techniques the electrode movement is also reconstructed, so the reconstructed image $\hat{\mathbf{x}}$ is of size $(n_N + n_D \cdot n_E)\times 1$, where the first n_N elements represent the conductivity changes and the rest electrode movements in each dimension. The reconstruction of the movement of the electrodes is valid as long as electrodes are assumed to have a small movement, as the Jacobian is linearised to zero electrode movement. Additionally, the movement is assumed to be a rigid body

translation[13], therefore if an electrode is modelled by several nodes they are assumed to have identical motion.

The size of the regularization matrix then has $n_D \cdot n_E$ additional columns and rows, and a separate hyperparameter is used for the regularization of the movement. In this work, as in [3], the ratio between the expected conductivity change against the expected electrode movement is set up to $\mu = 20$, while the regularization term itself is set to the value ensuring equal NF with the rest of the algorithms. With the value of the second model hyperparameter the regularization matrix can be described as $\mathbf{R} = \mathbf{R}_c + \mu^2 \mathbf{R}_m$. Then a supposition of smoothness in the electrode movement is applied, in addition to a penalty for non-zero movement in the electrodes. The regularization matrix with all the previous definitions is represented by

$$\mathbf{R}_{i,j} = \begin{cases} n_D + 1 & \text{if } i = j \text{ and } i \leq n_N \\ -1 & \text{if element } i \text{ is adjacent to } j \text{ and } i \leq n_N \\ 2.1\mu^2 & \text{if } i = j \text{ and } i > n_N \\ -\mu^2 & \text{if element } i \text{ is adjacent to } j \text{ and } i > n_N \\ 0 & \text{otherwise.} \end{cases} \tag{4}$$

This imaging technique is called "Laplace prior simultaneous" in this study for abbreviation. The 2.1 value ensures that there is non-zero penalty for equally moving electrodes.

In the simultaneous reconstruction techniques the new location of the electrodes is to be reconstructed. However, due to the so called "conformal problem"[14], it is not possible. Only the non-conformal part of the electrode displacement can be reconstructed. That means the smoothness supposition for the displacements of the electrodes may not necessarily apply.

Therefore an alternative approach to regularize only for the amplitude of the electrode movement is presented. This means that instead of using Laplace prior for the regularization, the Tikhonov approach is extended to the electrode movement section of $\mathbf{R}$. The regularization matrix is defined as

$$\mathbf{R}_{i,j} = \begin{cases} 1 & \text{if } i = j \text{ and } i \leq n_N \\ \mu & \text{if } i = j \text{ and } i > n_N \\ 0 & \text{otherwise.} \end{cases} \tag{5}$$

for the Tikhonov regularization approach in both conductivity and electrode displacement. λ and μ are the regularization parameters of values 0.01 and 16 respectively. The choice of this values comes from [12], where for a similar regularization approach these values give the best result. This imaging approach is referred as "Tikhonov prior simultaneous".

2.1.3 Tracked boundary

The other method that is analysed in this study is the use of having a boundary tracking device that measures the boundary at each imaging step. The idea of measuring the boundary has been analysed by Khor *et al*[15] previously. In that study, a wearable shape estimating sensors are presented, in order to get a more accurate description of the boundary. The idea of the image reconstruction method described here is to use the tracked shape not only for the improvement of the forward model, but also the inverse problem.

For the reconstruction algorithm a FEM mesh of each measured boundary in each position is generated, and a Jacobian is computed for each of these meshes. Additionally a reference uniform background measurement is simulated in each mesh. For each image, the Jacobian and reference background simulated measurement representing the current geometry are used in equation (3). Then, equation (3) can be rewritten as

$$\hat{\mathbf{x}} = (\mathbf{J}_k^t \mathbf{J}_k + \lambda^2 \mathbf{R})^{-1} \mathbf{J}_k^t (\mathbf{v}i_k - \mathbf{v}h_k) \tag{6}$$

where the sub-index k refers at the shape at time t_k and $\mathbf{v}i_k$ is the measured voltage and $\mathbf{v}h_k$ the simulated one using the forward solver. This, while computationally very expensive in comparison to the other algorithms, linearises the boundary movement problem to the current geometry, reducing artefacts. Standard Tikhonov regularization is used here, using the same values as in section 2.1.1. This method is referred a "Tracked boundary".

2.2 Performance figures of merit

During the evaluation of the boundary effects in lung imaging quantitative parameters are used. First, the commonly known GREIT parameters[7], that show the quality of the reconstructed target. Additionally, some global image quality parameters are used, adopted from image processing literature [16][17].

2.2.1 GREIT figures of merit

For the evaluation of the performance of reconstructions six performance figures of merit were defined[7]. In here, those figures of merit have been slightly modified, in order to be able to use them for multiple non-circular inclusions. From the six GREIT figures, five of them have been used for the evaluation of the results, while the sixth one (noise amplification) is used for regularization parameter selection, ensuring comparable results. The definition of the first five performance figures of merit with their small modifications are presented in figure 1.

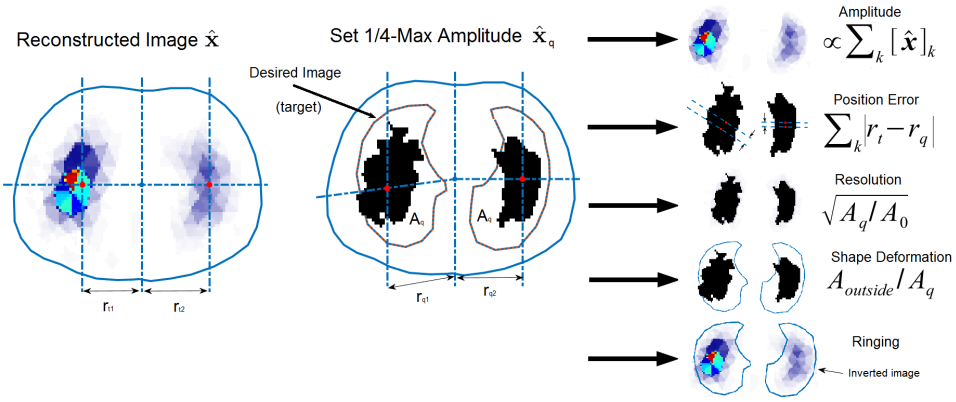

Figure 1: Target Amplitude, position error, resolution, shape deformation and ringing performance figures of merit for lung imaging.

For the first step, a new image is calculated from the reconstructed image $\hat{\mathbf{x}}$, where the pixels are defined as:

$$[\hat{\mathbf{x}_q}]_i = \begin{cases} 1 & \text{if } [\hat{\mathbf{x}}]_i \geq \frac{1}{4}\max(\hat{\mathbf{x}}) \\ 0 & \text{otherwise.} \end{cases} \tag{7}$$

Then, the six performance figures of merit are calculated for the image. These figures are:

- Target Amplitude measures the sum of pixel amplitudes in the reconstructed image.

$$\text{TA} = \sum_k [\hat{\mathbf{x}}_q]_i \tag{8}$$

  TA is the sum of all pixels in the image. It can be seen as a measure of the reconstruction gain. This parameter is similar to AR in GREIT, which is additionally normalized.

- Position error (PE) measures how precisely the centre of gravity of the target is obtained in the reconstruction. PE is defined as

$$\text{PE} = |r_t - r_q| \,. \tag{9}$$

  Where r_t and r_q are the reconstructed and the original centroids of the targets, respectively. For multiple objects, the average of them is computed. If the thresholding does not show all of them, PE is not defined. PE should be small and with small variability.

- Ringing (RNG) measures if the reconstructed target shows areas of opposite sign around the target itself.

$$\text{RNG} = \sum_{k \notin C \& [\hat{\mathbf{x}}]_k < 0} [\hat{\mathbf{x}}]_k \Big/ \sum_{k \in C} [\hat{\mathbf{x}}]_k, \tag{10}$$

  being C the true shape of the inclusions. For lungs, RNG can not be computed unless the true shape of the inclusion is known, making in unusable in a real application. However, it is useful in this study for algorithm evaluation purposes. RNG should be low and uniform.

- Resolution (RES) measures the size of the reconstructed target as a fraction of the medium.

$$\text{RES} = \sqrt{\frac{A_q}{A_0}} \tag{11}$$

- Shape deformation (SD) measures the fraction of the reconstructed $\frac{1}{4}$ Amplitude set which does not fit within the boundary of the original shape and same reconstructed area.

$$\text{SD} = \sum_{k \notin C} [\hat{\mathbf{x}}_q]_k \Big/ \sum_k [\hat{\mathbf{x}}_q]_k. \tag{12}$$

- Noise amplification (NF) measures how much random noise in the measurements is reconstructed in the image.

$$\text{NF} = \frac{E[\text{mean}|\hat{\mathbf{x}}_t|]/E[\text{std } \hat{\mathbf{x}}_n]}{E[\text{mean}|\mathbf{y}_t|]/E[\text{std } \mathbf{y}_n]}, \tag{13}$$

where y_t and x_t are the measured data and reconstructed image respectively and y_n and x_n are noisy data and the reconstructed image using that noisy data. NF has been used mainly for hyperparameter selection, not in performance evaluation.

2.2.2 Global parameters for figures of merit

In general it is difficult to find objective image quality evaluation parameters in EIT due to the complexity of the images and image reconstruction. Some attempts have been made to define a precise objective quality measurement e.g. for real time monitoring of the quality of the data [18]. In this work, in addition to the GREIT figures of merit, which were initially designed for circular targets, additional performance figures of merit are used, taken from signal and image processing literature. These parameters, instead of focusing on the quality of the target, give an overall value of the reconstruction quality. These parameters complement the GREIT parameters. They are useful here because a uniform value for the whole image would mean that the reconstruction is invariant in different breathing stages, which is the main thing that this study aims to evaluate. To perform the evaluation a black and white "target" image is created using the true shape of the modelled geometry and inclusions (lungs) and compared with the result of the reconstruction. Then the results of the reconstruction are converted to a 101x101 pixel square mesh, and normalized between 0-255. The parameters used are the following:

- **Pearson's correlation coefficient**. This is one of the most common coefficients for similarity. For two grayscale images X, Y, the correlation is defined by:

$$\rho_{X,Y} = \frac{\text{cov}(X,Y)}{\sigma_X \sigma_Y}, \tag{14}$$

were *cov* is covariance, and σ_X and σ_Y are standard deviations of the pixel values.

- **Normalized Mutual Information**. Mutual information is an entropy-based similarity evaluation parameter. It measures the dependency between two variables using Shannon's entropy[19]. Recently this coefficient has been used in EIT by Crabb *et al*[12] and is defined as:

$$I_{X,Y} = H(X) + H(Y) - H(X,Y) \tag{15}$$

or

$$I_{X,Y} = \sum_x \sum_y \mathrm{p}_{X,Y}(x,y) \log \frac{\mathrm{p}_{X,Y}(x,y))}{\mathrm{p}_X(x)\mathrm{p}_Y(y)}, \tag{16}$$

where H is Shannon's entropy, $p_X(x)$ and $p_Y(y)$ are the marginal probability distributions of data X and Y, respectively, and $p_{X,Y}(x,y)$ is the joint probability distribution. The numerical value of $I_{X,Y}$ is normalised by $H(X)$, X being the reference image with highest entropy. Unlike the correlation coefficient, mutual information can describe non-linear relationships between data, therefore being more reliable than correlation.

- **Sharpness of the image**. Even if mutual information and correlation give clear quality measurement coefficients, sometimes they can have a misleading value. If a result is very smooth and has not obtained the shape of the target properly, but is contained inside the area where the target should be, mutual information and correlation are higher than a case where the shape has been better reconstructed but is bigger than the original target. Due to this effect a sharpness coefficient has been chosen to evaluate the images. This coefficient gives additional information in order to characterize this effect. The sharpness of the image is obtained by convolving a Laplacian of Gaussian kernel to it, defined as:

$$\mathrm{LoG}(x,y) = \frac{1}{\pi\sigma^4}\left(\frac{x^2+y^2}{2\sigma^2} - 1\right) e^{-\frac{x^2+y^2}{2\sigma^2}}, \tag{17}$$

were σ is a scale parameter, in this work of value 5; and x and y refer here to the rows and column intensity values of a pixelated image. The reason of not applying the Laplacian high pass filter directly is to avoid the error that can be created by a local noisy pixel. To get a unique value for sharpness

$$\mathrm{Sharpness} = max(\mathrm{LoG}(img)) \tag{18}$$

is used.

2.3 Breathing simulation and evaluation procedure

To analyse the boundary movement in EIT lung imaging, an electrode movement effect and reconstruction test has been designed. Similar studies have been also made in the past[5]. Adler *et al*[6] proposed an

equation for chest movement, defined as:

$$\overline{d} = M\left[(y - y_c)\overline{y} + L\frac{APD}{LD}(x - x_c)\overline{x}\right], \tag{19}$$

where L is the ratio between lateral and anterior-posterior (AP) movement, APD is the anterior-posterior dimension and LD the lateral dimension, (x_c, y_c) is the coordinate of the center of the thorax, and $\overline{x}$ and $\overline{y}$ are unit vectors in the x and y direction. M is the movement fraction in the AP direction.

Recently, a more intensive study of how the electrode position varies in supine breathing has been performed by Zhang *et al*[4]. There, electrode position markers were painted on the body of several patients undertaking CT scans, and then the displacement of the markers due to breathing was measured. Although different studies have measured electrode movement, the results in this last one show that the respiration displacement for supine position and quiet, shallow respiration is lower than expected (%2 of the AP direction against %10 in the previously mentioned studies). The research involving geometrical properties of the thorax expansion is limited by the lack of in vivo measurements of the electrode movement. Therefore, in our case, the in vivo measurements performed in that study are used.

The FEM models are created using the 3D forward 2D inverse approach as in Grychtol *et al*[8]. A 3D forward fine model of the thorax with around 30K elements is built using patient data from EIDORS[20] and a 2D coarse model with around 2K elements is used for inverse reconstruction, as seen in figures 2 and 3. This meshing approach simulates current flow through the medium more realistically (as inner thorax currents do not only travel in the 2D plane) and solving only a 2D image speeds up the inverse calculation, as with a single electrode ring the amount of obtainable information in the perpendicular to the electrodes axis is small. This approach is commonly called 2.5D[21]. The FEM models have been computed using NETGEN mesher[22]. Ideally, several CT images with different thorax geometries would be simulated, but the study is already quite extensive, and extra models could overcomplicate the analysis of the results.

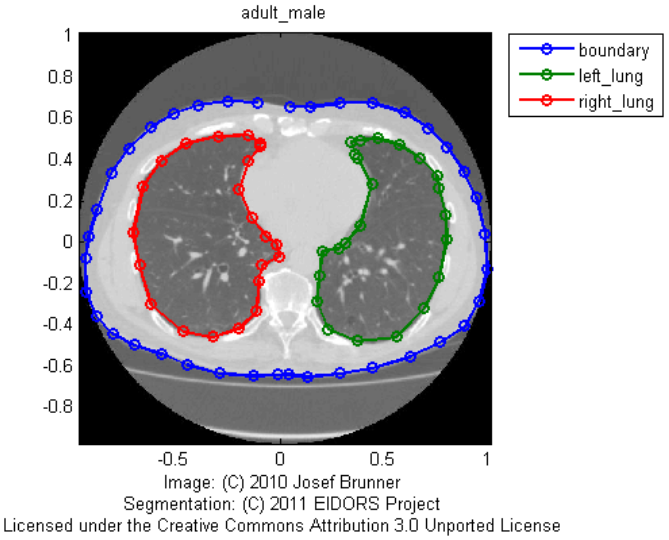

Figure 2: A lung healthy 49 year old adult male of average build CT slice and boundaries.

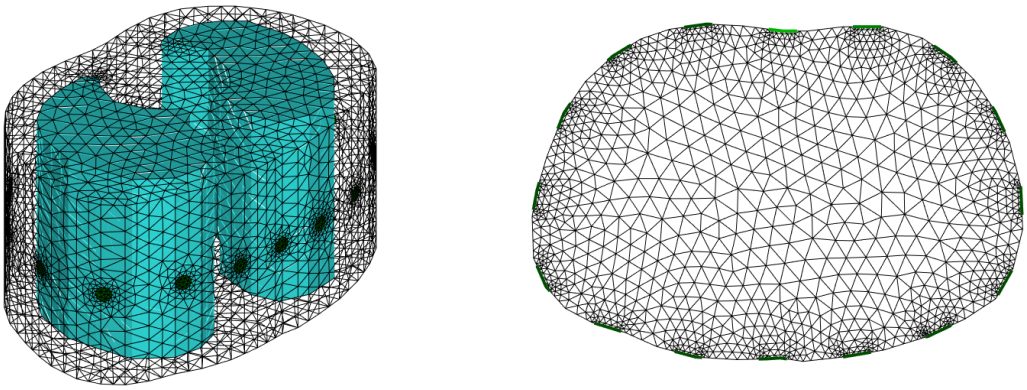

Figure 3: 3D and 2D fine and coarse models with human thorax shape used in the evaluation.

Then, the breathing of a patient in supine position is simulated. Equation (19) has been used, showing good enough correlation with the data profile of real measurements presented in [4]. The following numerical values are used in equation 19, taken from the in vivo measured values: anterior posterior dimension APD of 20.2 cm and lateral dimension LD 34.3 cm in the Functional Residual Capacity of the lungs (expiration in shallow breathing). The ratio between both dimensions, L is set to -0.5, as, unlike in upright position, in supine position the anterior-posterior direction expands during inspiration, but the lateral contracts. For the value of M (the percentage of movement in the AP direction), in Zhang *et al* it goes just up to 0.03 in quiet breathing, however to be consistent with the literature and other studies, an M up to 0.1 (10% of AP size) is simulated, as even if shallow breathing does not expand that much, the human chest can reach that expansion rate[23]. To create this movement steps in a mesh, 35 steps are simulated, 30 in the realistic movement situation and 5 in the non-realistic

area (10%-30%). The movement is applied to the boundary shape and then a new mesh is generated for each of these steps. To evaluate the robustness of the algorithms the same conductivity change is simulated in all breathing steps. This is an unrealistic scenario, but helps to analyse the performance of the algorithms with higher precision. The simulated conductivity value for the lungs is set up to $\sigma = 0.3$ for all steps.

The four different reconstruction methods explained in section 2.1 are performed in order to compare and evaluate the effect of electrode movement. All of them use uniform background as prior, and have 10% of the standard deviation of the difference data normal random measurement noise added. Finally, GREIT and image processing performance figures of merit are computed for each algorithm in each breathing movement step.

3 Results

3.1 Movement effect with true initial shape

As previously explained, four algorithms have been tested for electrode movement. The simulations have been performed starting with a perfectly known boundary and deforming that boundary with real patient measured chest movement. The reconstruction without movement, 3% of boundary size movement (expected value), 10% of boundary size movement (maximum value for human thorax) and 30% of boundary size movement (non-realistic case for evaluation purposes) are shown in figure 4. The image shows the four discussed reconstruction algorithms (columns) against increasing magnitude in the simulated breathing (rows). The rows represent movement of 0% , 3% (maximum measured in vivo shallow breathing), 10% (approximate physical limit of the human thorax) and 30% (unrealistic movement).

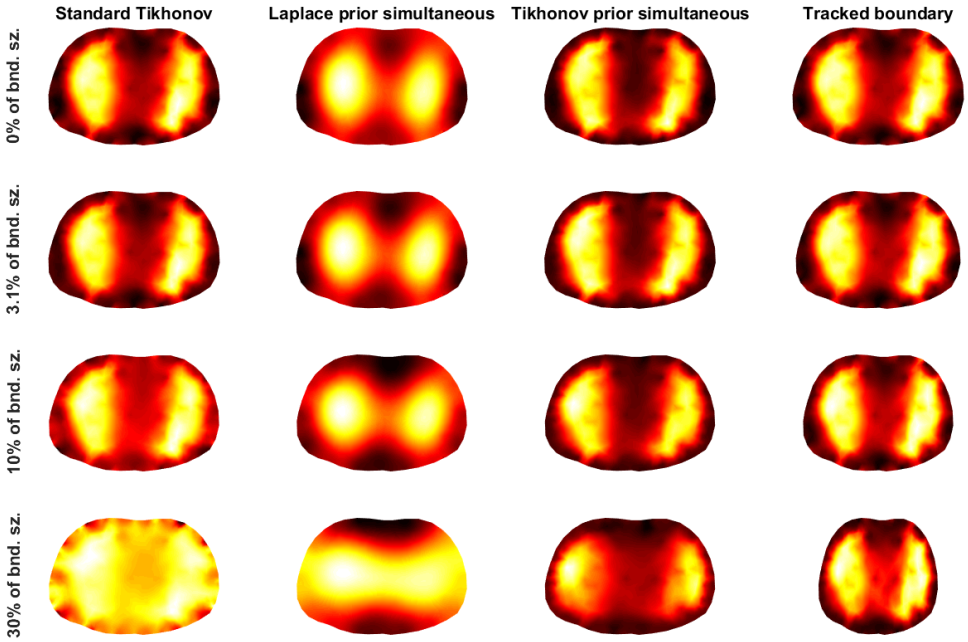

Figure 4: Standard Tikhonov, Laplace prior simultaneous, Tikhonov prior simultaneous and Tracked boundary reconstruction for boundary movement of 0% (no shape mismatch), 3% (expected maximum shape mismatch), 10% (upper limit for thorax expansion) and 30% (pushing the limit for evaluation). Calculations assume movement from a perfectly known initial boundary.

In figure 5 the three previously discussed image processing quality evaluation parameters are shown, plotted against the movement steps, from 0% to 30%, showing the errorbars of 50 different normal random noise in the measurements. The difference in uniformity is clear between the algorithms that take into account the motion and the one that does not. Additionally, the effect of not knowing the correct shape is observed for a movement of more than 10%, where the performance of all methods drop. In figure 6, the GREIT performance figures of merit are shown for the four reconstruction methods. Although in general uniformity is similar for all algorithms, their values vary. Generally, Laplace prior simultaneous reconstruction stands out (due to the different conductivity regularization approach). To evaluate the robustness of the algorithms against movement, the coefficient of variation (standard deviation divided by the mean) of the figures of merit is computed, as seen in table 1. As random noise has been added to the data, the results shown in the table are the average and standard deviation over 50 different noise samples. The most robust algorithms have the lowest coefficient of variation. The minimum values of coefficient of variation for each figure of merit are highlighted. Its important to note that PE is not

evaluated, as it is not defined in all the movement steps (sometimes there are less than 2 defined targets in the reconstructed image).

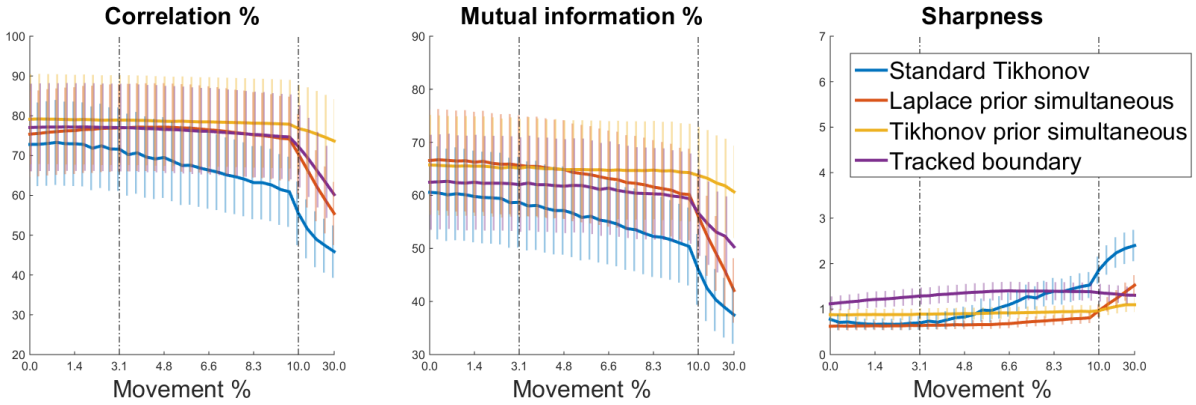

Figure 5: Mean and standard deviation of correlation, mutual information and sharpness results for 35 linear steps of human breathing movement, from 0 to 30% of the AP size. Calculations assume movement from a perfectly known initial boundary. Note that the errorbars have a slight offset just for visualization purposes.

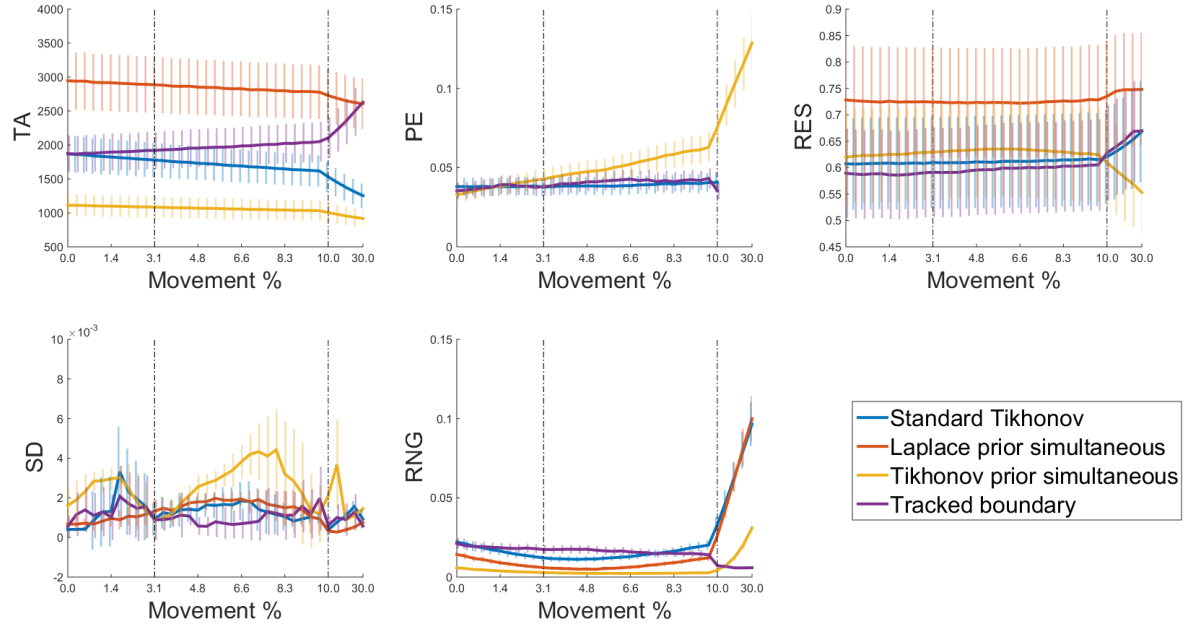

Figure 6: Mean and standard deviation of GREIT performance figures of merit for 35 linear step of human breathing movement, from 0 to 10% of the AP size. Calculations assume movement from a perfectly known initial boundary. Note that the errorbars have a slight offset just for visualization purposes.

	Standard Tikhonov.	Laplace simult.	Tikhonov simult.	Tracked boundary.
TA	0.0448 ± 0.0015	0.0198 ± 0.0017	0.0242 ± 0.0015	0.0290 ± 0.0014
RES	0.0069 ± 0.0010	0.0053 ± 0.0007	0.0085 ± 0.0007	0.0117 ± 0.0011
SD	0.8759 ± 0.0991	0.4816 ± 0.0547	0.6309 ± 0.0557	1.0006 ± 0.1003
RNG	0.2277 ± 0.0148	0.3592 ± 0.0244	0.3305 ± 0.0267	0.1231 ± 0.0119
Corr.	0.0631 ± 0.0054	0.0342 ± 0.0023	0.0104 ± 0.0012	0.0193 ± 0.0020
Mutual info.	0.0651 ± 0.0042	0.0123 ± 0.0008	0.0061 ± 0.0005	0.0109 ± 0.0005
Sharp.	0.3510 ± 0.0201	0.0944 ± 0.0070	0.0365 ± 0.0040	0.0719 ± 0.0035

Table 1: Mean coefficient of variation and standard deviation of 7 of the figures of merit defined in the document against the 4 tested image reconstruction methods. 50 tests with random Gaussian noise were performed. Electrode movement is present and correct initial shape is known. The smallest values are highlighted.

To perform a full analysis of a realistic situation, all the undesired effects should be evaluated together, as due to the ill-possessedness of the problem, effects cannot be assumed to have similar behaviour when put together. The evaluation procedure is exactly the same as in the previous section, with a minor change. The voltages are simulated with a specific thorax shape and the inverse solution are computed with Jacobians of a different shape. Both shapes can be seen in figure 7. The different shape has been chosen so it is located in the "uniform behaviour" section of the algorithms. The tolerable shape mismatch was evaluated by Grychtol *et al* [8] to be 4% of normalized area difference. This approach is supposed to simulate a more realistic situation, where an approximate knowledge of the shape is known, but not with 100% of accuracy. The process to obtain the boundary from the image goes as follows: The image is threshold with Otsu's method[24], eroded and dilated, filled with flood-fill algorithm[25] and finally keeping the biggest blob, whose boundary is obtained and used to create a FEM model.

Figure 7: Two different CT scans of different patients and their two boundaries plotted together. The second one was chosen inside the shape mismatch tolerance studied by Grychtol *et al*[8].

The same performance figures of merit are computed in this case, for al the reconstructed images seen in 8. The image processing figures of merit are shown in figure 9 and the GREIT figures in figure 10. In figure 9, the higher uniformity of tracked boundary can be observed, and the effect of not taking into account the electrode movement is also visible. The coefficient of variation of the figures of merit are calculated in table 2.

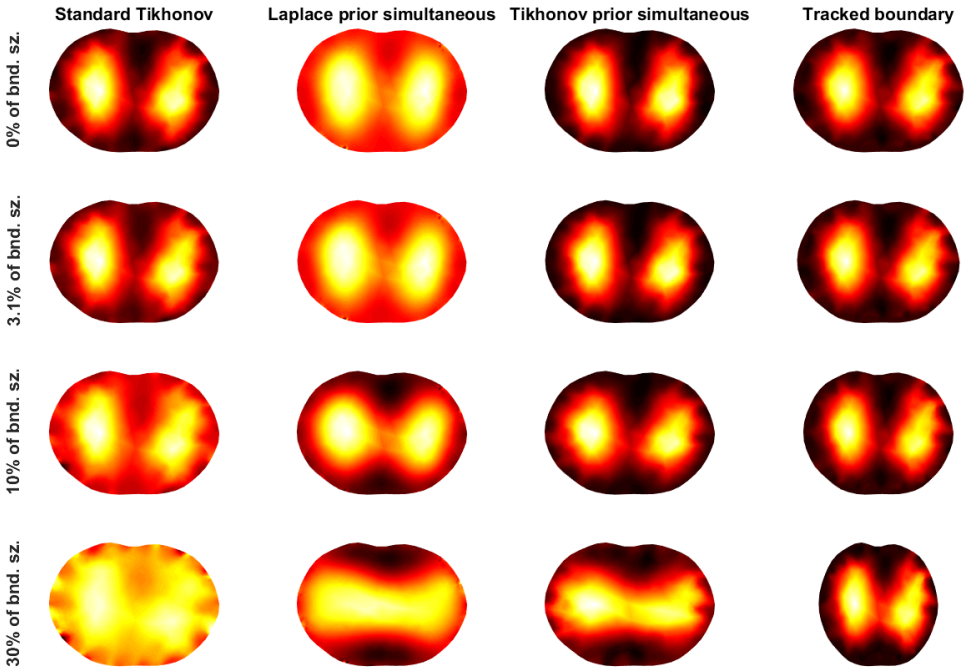

Figure 8: Standard Tikhonov, Laplace prior simultaneous, Tikhonov prior simultaneous and Tracked boundary reconstruction and shape correction reconstruction for boundary movement of 0% (no shape mismatch), 3% (expected maximum shape mismatch), 10% (upper limit for thorax expansion) and 30% (pushing the limit for evaluation). Electrode movement and shape mismatch are both present.

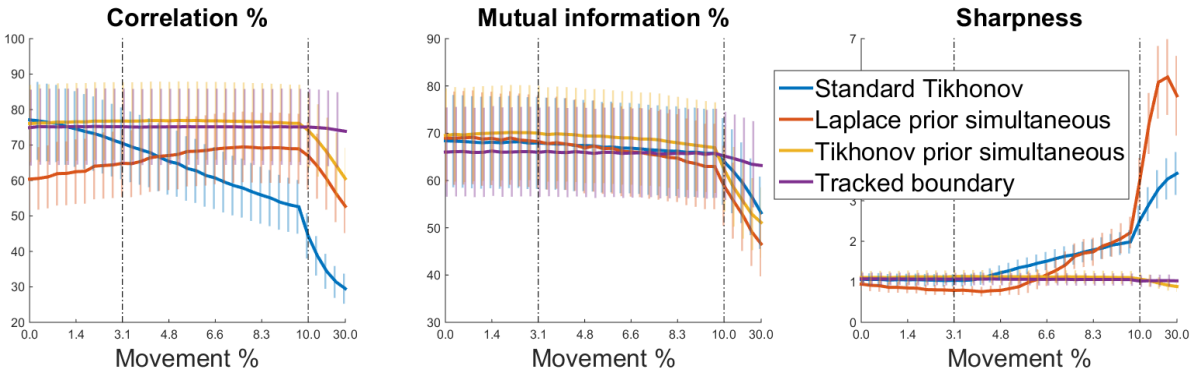

Figure 9: Mean and standard deviation of correlation, mutual information and sharpness results for 35 linear steps of movement, from 0 to 10% of the AP size. Electrode movement and shape mismatch are both present. Note that the errorbars have a slight offset just for visualization purposes.

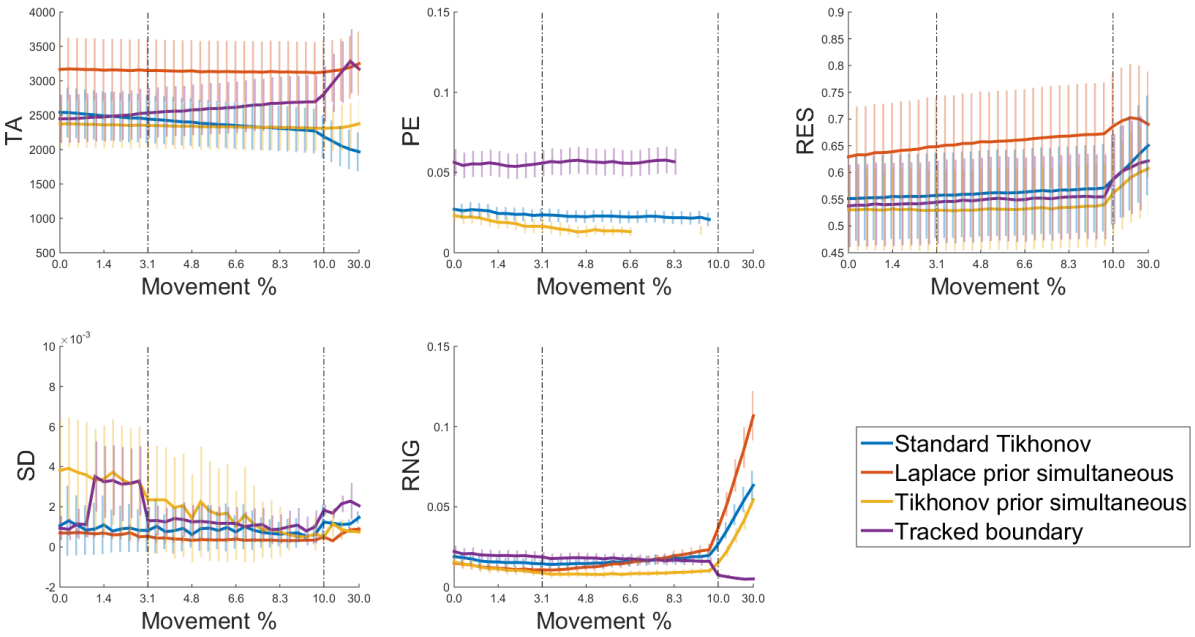

Figure 10: Mean and standard deviation of GREIT performance figures of merit for 35 linear step of human breathing movement, from 0 to 10% of the AP size. Electrode movement and shape mismatch are both present. Note that the errorbars have a slight offset just for visualization purposes.

	Standard Tikhonov.	Laplace simult.	Tikhonov simult.	Tracked boundary.
TA	0.0358 ± 0.0016	0.0106 ± 0.0013	0.0126 ± 0.0015	0.0328 ± 0.0015
RES	0.0139 ± 0.0014	0.0206 ± 0.0015	0.0116 ± 0.0016	0.0131 ± 0.0013
SD	1.1472 ± 0.2944	0.4645 ± 0.0750	1.1634 ± 0.1168	0.8759 ± 0.0738
RNG	0.1431 ± 0.0155	0.2684 ± 0.0159	0.2689 ± 0.0333	0.1265 ± 0.0162
Corr.	0.0151 ± 0.0013	0.0311 ± 0.0025	0.0161 ± 0.0017	0.0109 ± 0.0014
Mutual info.	0.1216 ± 0.0022	0.0512 ± 0.0038	0.0049 ± 0.0005	0.0033 ± 0.0005
Sharp.	0.2500 ± 0.0064	0.4211 ± 0.0217	0.0215 ± 0.0028	0.0132 ± 0.0020

Table 2: Mean coefficient of variation and standard deviation of 7 of the figures of merit defined in the document against the 4 tested image reconstruction methods. 50 tests with random Gaussian noise were performed. Both electrode movement and shape mismatch are present. The smallest values are highlighted.

4 Discussion

The aims of the present study was to evaluate if a boundary tracking device would enhance robustness against electrode movement and shape mismatch in lung imaging. With this question in mind, the sensitivity of various algorithms to the boundary movement have been examined, simulating realistic breathing-related movement in expected, possible and unrealistic scenarios.

The use of boundary shape tracking and creating a changing reference data (with uniform conductivity) and an updated Jacobian matrix produced satisfactory reconstruction results. This updating of the reference point and updating the Jacobian matrix in various step of EIT data collection (and simultaneous shape data) is reducing the non-linearity effects and does not include any mode error. Although performing very well, a shape tracking and update of reference data and Jacobian is computationally costly.

It is important to note that the uniformity assumption in EIT imaging introduces sources of error in lung imaging[26]. In the present study, the conductivity simulated on all steps has been the same, so it can be argued that the errors due to homogeneous background assumptions will introduce the same error in all the simulations, thus leaving unmodified the standard deviations analysed in the study. Additionally, errors due to re-meshing of the models for each movement step are present in the study[27]. As the mesh density does not change for each FEM model, these errors are assumed to be small.

While looking at the values of the performance figures of merit, in both GREIT and the image processing parameters, one of the most important feature an algorithm must manifest in this experiment is uniformity over time, in contrast to Grychtol *et al*[8], where spatial uniformity was the focus. The uniformity of the parameter ensures similar reconstruction for different states of the breathing pattern, or in other words, more robustness against movement. Therefore, the most robust algorithms are the ones that have smaller coefficient of variation in the figures of merit for different mismatch. While this is true for robustness of the algorithms against the effects studied, the value of the parameters studied are important for the quality of the resulting images.

In table 1 the minimum values of the coefficients of variation are more distributed in general. However in the most realistic scenario, when both shape mismatch and electrode movement are present, tracked boundary algorithm has the best performance, as seen in table 2.

However, it can be also appreciated that using simultaneous reconstruction algorithms has higher robustness than not accounting for electrode movement. This performance can also be seen in figures 4 and figure 8. The simultaneous reconstruction algorithms can reduce the effect of the strong non-linear effect of shape on the reconstruction.

The simultaneous reconstruction methods aim to obtain the movement of the electrodes, but they cannot be reliably used for measuring electrode movement due to the known "conformal problem". As the electrode movement cannot be correctly reconstructed, assuming smoothness as a prior is not realistic, as the obtainable results will not necessarily be smooth (only the non-conformal part of the movement can be obtained). That may be why the Tikhonov prior simultaneous algorithm has better results in the overall image robustness, than the Laplace prior simultaneous method.

The study has been performed using 2.5D models, therefore it is safe to say that this study applies to single plane electrode lung imaging. Possibly more complicated effects are created in multiple ring lung imaging, but that would need a further study.

The study shows an approximate movement simulation of the electrodes based on clinically measured data, however, the movement is purely in-plane. With different body types, the electrode movement may move in an out-of-plane direction, increasing the artefacts in the reconstruction. The proposed algorithms for the correction of the electrode movement errors are three dimensional, therefore the out-of-plane displacement can also be algorithmically taken into account in the three dimensional case.

One of the limitations of the study is the choice of adult human thorax model for the simulations. EIT is also used in neonatal lung monitoring, where the size of the electrodes and the gap between them have widely different proportions than in adult patients. Most likely, the errors due to shape deformation and electrode movement increase in neonatal lug monitoring, making it more important to account for these effects.

Lastly, one of the problems in practical EIT lung imaging is that ECG electrodes may migrate during the treatment. This unknown electrode position effect will clearly increase the error in reconstruction, and depending in the amount of displacement it could even degenerate the quality of the result until the point of making it impossible to read. Our study is limited to the evaluation of the effect of breath and unknown exact shape in lung EIT imaging, therefore the possible migration of the electrodes have not been taken into account.

5 Conclusions

The effect of normal breathing should be considered in lung EIT imaging. However, the study shows that the artefacts are not very big in shallow supine breathing. While all algorithms show good performance without shape mismatch, once both shape and movement error effects are combined, a higher level of artefacts arise. The best performing image reconstruction in our study is the tracked boundary reconstruction algorithm, but the computational overhead is likely too high for real time imaging.

Alternatively, if the extra computational time is not desired, the simultaneous reconstruction methods are recommended. Using the simultaneous reconstruction with standard Tikhonov regularization shows better results, as the assumption of smoothness is not consistent with reconstruction ability of the electrode movement Jacobian. Similarly to other studies, we conclude that it is important to develop patient specific models in lung EIT, with the highest possible accuracy in the outer boundary.

As future work, the same study for a range of patient thorax geometries could be interesting, in order to ensure that the effects are model independent. In addition, the study could extend to 3D EIT imaging with multiple electrode layers, where the errors due to shape mismatch and electrode movement are expected to be higher. The approximation error model (AEM) based algorithm could be evaluated.

As a final conclusion, in EIT lung imaging boundary movement due to breathing should not imply a significant problem to constrain the ability of reconstructing high quality images, even with some small shape mismatch. We demonstrated possible advantage of a shape tracking system and implementing that in an image reconstruction process by updating the Jacobian matrix and moving reference data.

References

[1] A. Adler, M. B. Amato, J.H. Arnold, R. Bayford, M. Bodenstein, H. Stephan Böhm, B.H. Brown, I. Frerichs, O. Stenqvist, N. Weiler, and G.K. Wolf. Whither lung EIT: Where are we, where do we want to go and what do we need to get there? *Physiological Measurement*, 33(5):679, 2012.

[2] D.C. Barber and B.H. Brown. Errors in reconstruction of resistivity images using a linear reconstruction technique. *Clinical Physics and Physiological Measurement*, 9(4A):101, 1988.

[3] M. Soleimani, C. Gómez-Laberge, and A. Adler. Imaging of conductivity changes and electrode movement in EIT. *Physiological Measurement*, 27(5):S103, 2006.

[4] J. Zhang, L. Qin, T. Allen, and R.P. Patterson. Human CT measurements of structure/electrode position changes during respiration with electrical impedance tomography. *Open Biomed Eng J*, 15(7):109–15, Nov 2013.

[5] J. Zhang and R.P. Patterson. EIT images of ventilation: what contributes to the resistivity changes? *Physiological Measurement*, 26(2):S81, 2005.

[6] A. Adler, R. Guardo, and Y. Berthiaume. Impedance imaging of lung ventilation: do we need to account for chest expansion? *Biomedical Engineering, IEEE Transactions on*, 43(4):414–420, April 1996.

[7] A. Adler, R. Arnold, J.H. an Bayford, A. Borsic, B. Brown, P. Dixon, T. J. C. Faes, I. Frerichs, H. Gagnon, Y. G´arber, B. Grychtol, G. Hahn, W.R.B. Lionheart, A. Malik, R.P. Patterson, J. Stocks, A. Tizzard, N. Weiler, and G.K. Wolf. GREIT: a unified approach to 2D linear EIT reconstruction of lung images. *Physiological Measurement*, 30(6):S35, 2009.

[8] B. Grychtol, W.R.B. Lionheart, M. Bodenstein, G.K. Wolf, and A. Adler. Impact of model shape mismatch on reconstruction quality in electrical impedance tomography. *Medical Imaging, IEEE Transactions on*, 31(9):1754–1760, Sept 2012.

[9] A. Adler and R. Guardo. Electrical impedance tomography: regularized imaging and contrast detection. *Medical Imaging, IEEE Transactions on*, 15(2):170–179, Apr 1996.

[10] M. Cheney, D. Isaacson, J.C. Newell, S. Simske, and J. Goble. NOSER: An algorithm for solving the inverse conductivity problem. *Int. J. Imaging Syst. Technol.*, 2:66–75, 1990.

[11] B. M. Graham and A Adler. Objective selection of hyperparameter for EIT. *Physiological Measurement*, 27(5):S65, 2006.

[12] M.G. Crabb, J.L. Davidson, R. Little, P. Wright, A.R. Morgan, C.A. Miller, J.H. Naish, G.J.M. Parker, R. Kikinis, H. McCann, and W.R.B. Lionheart. Mutual information as a measure of image quality for 3D dynamic lung imaging with EIT. *Physiological Measurement*, 35(5):863, 2014.

[13] C. Gómez-Laberge and A. Adler. Direct calculation of the electrode movement jacobian for 3D EIT. In Hermann Scharfetter and Robert Merwa, editors, *13th International Conference on Electrical Bioimpedance and the 8th Conference on Electrical Impedance Tomography*, volume 17 of *IFMBE Proceedings*, pages 364–367. Springer Berlin Heidelberg, 2007.

[14] A. Boyle, A. Adler, and W.R.B. Lionheart. Shape deformation in two-dimensional electrical impedance tomography. *Medical Imaging, IEEE Transactions on*, 31(12):2185–2193, Dec 2012.

[15] J.M. Khor, A Tizzard, A Demosthenous, and R Bayford. Wearable sensors for patient-specific boundary shape estimation to improve the forward model for electrical impedance tomography (EIT) of neonatal lung function. *Physiological Measurement*, 35(6):1149, 2014.

[16] Wilhelm Burger and Mark J. Burge. *Principles of Digital Image Processing, Fundamental techniques.* Springer, 2009.

[17] D.B. Russakoff, C. Tomasi, T. Rohlfing, and Jr. Maurer, C.R. Image similarity using mutual information of regions. In Tom Pajdla and Ji Matas, editors, *Computer Vision - ECCV 2004*,

volume 3023 of *Lecture Notes in Computer Science*, pages 596–607. Springer Berlin Heidelberg, 2004.

[18] Y. Mamatjan, B. Grychtol, P. Gaggero, J. Justiz, V.M. Koch, and A. Adler. Evaluation and real-time monitoring of data quality in electrical impedance tomography. *Medical Imaging, IEEE Transactions on*, 32(11):1997–2005, Nov 2013.

[19] C.E. Shannon. A mathematical theory of communication. *Bell System Technical Journal*, 27(1):379–423,623–656, 1948.

[20] A. Adler and W.R.B. Lionheart. Uses and abuses of EIDORS: an extensible software base for EIT. *Physiological Measurement*, 27(5):S25, 2006.

[21] N. Bahrani and A. Adler. 2.5D finite element method for electrical impedance tomography considering the complete electrode model. In *Electrical Computer Engineering (CCECE), 2012 25th IEEE Canadian Conference on*, pages 1–6, April 2012.

[22] J. Schöberl. NETGEN an advancing front 2D/3D-mesh generator based on abstract rules. *Computing and Visualization in Science*, 1(1):41–52, 1997.

[23] J.M. Moll and V. Wrighr. An objective clinical study of chest expansion. *Ann Rheum Dis*, 31(1):1–8, Jan 1972.

[24] N. Otsu. A threshold selection method from gray-level histograms. *Systems, Man and Cybernetics, IEEE Transactions on*, 9(1):62–66, Jan 1979.

[25] Pierre Soille. *Morphological Image Analysis: Principles and Applications*. Springer-Verlag New York, Inc., Secaucus, NJ, USA, 2 edition, 2003.

[26] B. Grychtol and A. Adler. Uniform background assumption produces misleading lung EIT images. *Physiological Measurement*, 34(6):579, 2013.

[27] A. Adler and W.R.B. Lionheart. Minimizing EIT image artefacts from mesh variability in finite element models. *Physiological Measurement*, 32(7):823, 2011.